This manuscript is a non-peer-reviewed preprint submitted to EarthArXiv

Robust Regional Predictability of North Atlantic Tropical Cyclones on Seasonal Timescale

Dan Fu[1*], Xue Liu[2], Frederic Castruccio[3], Stephen Yeager[3], Gokhan Danabasoglu[3], Ping Chang[1,2]

[1]Department of Atmospheric Sciences, Texas A&M University, College Station, Texas, USA

[2]Department of Oceanography, Texas A&M University, College Station, Texas, USA

[3]National Science Foundation National Center for Atmospheric Research, Boulder, Colorado, USA

*Corresponding author. Email: fudan1991@tamu.edu; ORCID: 0000-0001-6423-6117

Abstract

Tropical cyclones (TCs) are intermittent extreme weather events, yet their seasonal occurrence can be constrained by slowly varying climate variability and regional predictability remains poorly understood. Using 44 years of May-initialized ensemble hindcasts, we show robust seasonal predictability of North Atlantic TC track density across two prediction systems with contrasting resolutions: nominal 1° versus 0.25° atmosphere/0.1° ocean. Both show similar skill over the Gulf region and Caribbean Sea, with correlations approaching 0.6, despite underestimated TC climatology in the low-resolution system. This predictability is linked to a large-scale sea surface temperature pattern predicted months in advance, with correlations exceeding 0.8, and associated atmospheric circulation changes. Yet similar observed skill arises from sharply contrasting model-internal signal-to-noise characteristics: weak ensemble-coherent TC variability in the low-resolution system but a stronger predictable signal in the high-resolution system. These results suggest that weak model signal-to-noise does not necessarily imply weak physical predictability for intermittent extreme weather.

Introduction

Tropical cyclones (TCs) pose severe wind, precipitation and coastal flooding hazards, creating a strong demand for information about seasonal activity before individual storms form (1, 2). The scientific basis for such forecasts is the influence of slowly varying climate conditions on atmospheric variability. In particular, large-scale sea surface temperature (SST) anomalies can modify the thermodynamic and dynamical environment in which TCs develop and move, providing information beyond the range of individual weather forecasts (3, 4). This principle was translated into Atlantic seasonal hurricane outlooks at Colorado State University (CSU) beginning in 1984, using empirical relationships between hurricane activity and large-scale climate indicators, including the El Niño–Southern Oscillation (ENSO), the stratospheric quasi-biennial oscillation (QBO) and sea-level pressure over the Caribbean Sea (1, 4, 5). Since then, seasonal TC forecasting has developed into an operational activity across multiple forecasting centers. These outlooks have traditionally focused on basin-integrated quantities, including the total number of named storms, hurricanes and major hurricanes, as well as accumulated cyclone energy (ACE). Assessments of these forecasts show that skill in basin-wide activity generally increases as the hurricane season

approaches, from relatively low skill in April to modest skill in June and substantially higher skill by August (1).

In parallel, dynamical seasonal TC prediction emerged through initialized coupled climate models, beginning with early forecasts at the European Centre for Medium-Range Weather Forecasts (ECMWF) (6, 7). Subsequent prediction systems, including the UK Met Office GloSea5 and higher-resolution GFDL models, demonstrated useful skill for North Atlantic TC frequency and ACE and extended dynamical forecasts to major hurricanes and landfalling activity (8–11). Despite these advances, seasonal TC prediction has remained largely focused on basin-integrated activity, whereas regional information is needed to assess geographically specific exposure (2, 12). Skill in basin-wide activity does not necessarily imply skill in the spatial distribution of TC occurrence. Regional track density reflects not only the total number of TCs, but also variations in genesis location, storm development and survival, and subsequent movement, and can therefore differ substantially between seasons with comparable basin-wide activity (13–15). Predicting these spatial variations therefore represents a distinct frontier in seasonal TC prediction and an important step toward translating seasonal climate predictability into regionally relevant information.

Earlier regional assessments suggest that spatially resolved TC prediction is feasible, but also reveal substantial uncertainty in its robustness. Useful skill has been reported across the western tropical Atlantic, Caribbean and adjacent North American coastal regions, although its magnitude and spatial extent vary with initialization month, verification period and prediction system (16, 17). Previous assessments have also been constrained by relatively short common hindcast periods, regional aggregation or rank-based measures of occurrence, while significant spatial skill is often concentrated within limited parts of the basin. These studies provide important evidence that regional TC variability contains a predictable component, but do not yet establish how robust that component is across models, lead times and verification frameworks.

A second uncertainty concerns the physical source of regional predictability. Large-scale SST variability, including ENSO and tropical Atlantic SST anomalies, is known to modulate Atlantic TC activity (18–21), but reproducing basin-wide climate–TC relationships does not guarantee that their regional spatial expression is represented correctly. European seasonal prediction models, for example, can capture the broad ENSO influence on Atlantic TC activity while misrepresenting its geographical structure, particularly over the Caribbean (22). More generally, improved prediction of TC-relevant environmental conditions does not necessarily translate into improved TC forecasts. Recent comparisons of GFDL prediction systems show that differences in the amplitude of interannual TC variability and in the sensitivity of TC activity to large-scale conditions can strongly affect forecast skill even when the large-scale environment itself is predicted well (11).

A third challenge is that model-internal predictability and observed prediction skill are not equivalent quantities. Ensemble-based measures quantify the strength of the predictable signal represented within a model, whereas forecast skill measures agreement with observed seasonal variations. Previous studies have shown that weak model signal-to-noise ratios can coexist with substantial observed skill, and that model-derived estimates of potential predictability need not directly represent the predictability realized in nature (23, 24). For regional TC occurrence, where the target itself is sparse and highly variable, this distinction becomes particularly relevant. It therefore remains unclear whether robust regional TC skill requires a strong ensemble-coherent signal, or whether different prediction systems can recover comparable observed predictability while representing the underlying predictable variability very differently.

Here we address these questions using observations and 44 years (1980–2023) of May-initialized hindcasts from two Community Earth System Model (CESM) based prediction systems: the High Resolution Decadal Prediction system (HRDP), which is based on CESM version 1.3 with ~0.25° resolution atmosphere and land components and ~0.1° resolution ocean and sea-ice components (25–27), and the Seasonal-to-Multiyear Large Ensemble (SMYLE), which is based on CESM version 2 with a nominal resolution of ~1° across all components (28) (Methods). Beyond their substantial difference in horizontal resolution, HRDP and SMYLE are built on different CESM generations and employ different atmospheric dynamical cores and physical parameterization suites, resulting in markedly different simulated TC climatology. These contrasts provide an opportunity to assess the robustness and physical basis of regional TC predictability across substantially different climate prediction systems.

Robust regional TC prediction despite contrasting climatology

The HRDP and SMYLE prediction system exhibit markedly different representations of TC climatology (Fig. 1a,d) but surprisingly similar patterns of seasonal prediction skill (Fig. 1b,e). HRDP captures the broad observed geographical distribution of TC activity, although notable regional biases remain, including underestimated activity over parts of the western North Pacific (WNP) and North Atlantic (NA) and overestimated activity in the eastern North Pacific (ENP; Supplementary Fig. 1a,b). In contrast, SMYLE exhibits much larger negative biases, substantially underestimating TC occurrence across the major Northern Hemisphere TC basins (Supplementary Fig. 1c). Consequently, HRDP simulates considerably more TC activity than SMYLE across most regions (Supplementary Fig. 1d), consistent with the well-established sensitivity of simulated TC activity to model resolution (29, 30).

Despite these pronounced climatological differences, both systems exhibit remarkably similar patterns of seasonal prediction skill. Using linearly detrended TC track density anomalies over 1980–2023, statistically significant positive anomaly correlation coefficients (ACCs) extend across large portions of the NA and North Pacific sector in both HRDP and SMYLE (Fig. 1b,e). Focusing on the NA, a particularly coherent region of skill emerges over the Gulf region and Caribbean Sea, where local ACCs approach 0.6. Remarkably, SMYLE shows comparable and even higher skill than HRDP over this region (Supplementary Fig. 2), despite its substantially larger negative bias in climatological TC activity. The regional skill is also largely insensitive to long-term trends, as ACCs calculated from the original, non-detrended time series exhibit very similar spatial patterns and magnitudes over the Gulf–Caribbean region, including the relative skill difference between the two systems (Supplementary Fig. 3). The persistence of this skill after removing linear trends demonstrates that it primarily reflects predictable interannual variations in regional TC activity rather than agreement arising from long-term changes.

The initialized forecasts also provide substantial skill beyond persistence (Fig. 1c,f). Positive differences in ACC extend across much of central Pacific and western NA in both systems, including the Gulf–Caribbean region, indicating that the regional skill cannot be explained simply by persistence of the preceding TC state. Taken together, the robust skill over 44 years of detrended verification, its consistency across two substantially different prediction systems, and improvement over persistence establish a predictable component in the spatial distribution of seasonal TC occurrence. The comparable regional skill despite markedly different TC climatology

further raises the question of whether HRDP and SMYLE represent the underlying predictable TC signal in the same way.

Signal-to-noise characteristics of regional TC prediction skill

However, the comparable regional prediction skill in HRDP and SMYLE masks substantial differences in their model-internal predictable signals. To quantify these differences, we calculate the signal-to-total ratio (S2T), which measures the amplitude of the ensemble-mean predictable signal relative to the total year-to-year variability represented within each prediction system (Methods). HRDP exhibits substantially larger S2T than SMYLE across much of the tropical Pacific and western North Atlantic, including the Gulf–Caribbean region (Fig. 2a,c). SMYLE, on the other hand, shows much weaker ensemble-coherent TC variability over many of the same regions where its observed ACC is comparable to, or even higher than, that of HRDP. Therefore, similar observed prediction skill can emerge from prediction systems with very different amplitudes of internally predictable TC variability.

This difference is further illustrated by the ratio of predictable components (RPC), defined as the forecast–observation ACC normalized by S2T (23, 24). Over much of the skillful Gulf–Caribbean region, HRDP exhibits RPC values close to one, indicating broad consistency between its model-internal predictable signal and observed prediction skill (Fig. 2b). In contrast, SMYLE exhibits RPC values substantially greater than one across much of the same region (Fig. 2d), which is recognized as "*signal-to-noise paradox*". This paradox was first highlighted prominently in seasonal predictions of the winter North Atlantic Oscillation (NAO), where the ensemble-mean forecast correlated well with observations despite a much weaker predictable signal within the model than would be expected from the observed skill (23, 31). In those NAO forecasts, increasing ensemble size substantially improved skill by reducing realization-specific noise and isolating the weak predictable component, motivating the broader interpretation that model-internal signal strength can underestimate the predictability realized in observations (23, 32–34).

The TC case here exhibits a related but physically distinctive condition. HRDP contains a relatively strong ensemble-coherent TC signal with RPC near unity over the Gulf-Caribbean region, whereas SMYLE achieves comparable or even higher prediction skill despite a much smaller S2T and RPC substantially above one. Given SMYLE's strongly low-biased and sparse TC climatology, such a weak ensemble-coherent signal is not unexpected. Regional TC track density is constructed from a relatively small number of discrete storms, so realization-to-realization differences in genesis, survival and tracks can strongly influence the modeled year-to-year variability, particularly when the mean TC frequency is already strongly underestimated. This intermittency can reduce the prominence of the ensemble-mean TC signal without necessarily eliminating the climate information that conditions regional TC frequency.

The comparison therefore highlights an important distinction between model-internal signal strength and actual forecast skill for highly intermittent extreme weather. A low modeled S2T does not necessarily imply low prediction skill against observations, just as a stronger ensemble-coherent signal does not automatically guarantee greater skill. In the present case, SMYLE's weak internal TC signal coexists with robust Gulf–Caribbean ACC, whereas HRDP produces a much stronger internal signal but only comparable observed skill. The magnitude of ensemble-coherent TC variability alone therefore cannot explain the regional prediction skill identified in Fig. 1. This

motivates the next question: whether both systems nevertheless capture a common large-scale climate influence associated with the observed regional TC variations.

A predictable large-scale SST pattern linked to regional TC variability

To identify a common source of the regional prediction skill, we apply singular value decomposition (SVD) between global SST and North Atlantic TC track density. In observations, the leading mode (SVD1) explains 60.4% of the total squared SST–TC covariance (Fig. 3a,b). The SST loading features a pronounced ENSO-like structure across the tropical Pacific together with a NA tripole pattern characteristic of SST variability presumably associated with the North Atlantic Oscillation (NAO) (35–37). The corresponding TC pattern is strongly concentrated over the Gulf–Caribbean region and western tropical North Atlantic, closely overlapping the region of prediction skill identified in Fig. 1.

Both prediction systems reproduce the major spatial features of this coupled variability (Fig. 3c–f). The leading mode accounts for 82.1% of the squared covariance in the 10-member ensemble mean HRDP and 97.2% in the 20-member ensemble mean SMYLE, indicating that the ensemble-mean SST–TC relationship is dominated by a single large-scale mode in both systems. These higher squared covariance fractions (SCFs) relative to observations partly reflect ensemble averaging, which suppresses atmospheric internal variability and isolates the covariance shared across members.

We therefore examine the sensitivity of the SVD structure to ensemble size (Fig. 4; Supplementary Figs. 4–7). With only one ensemble member, the median SVD1 SCF is already 51.3% in HRDP and 62.5% in SMYLE, comparable to the observed value of 60.4%. Meanwhile, the median spatial correlations with the observed SVD1 patterns are approximately 0.55 and 0.76 for SST and 0.62 and 0.81 for TC in HRDP and SMYLE, respectively (Fig. 4b,c). This suggests that both systems retain an observed-like leading SST–TC covariance structure even at the single-realization level, increasing confidence that the strong coupled mode in the ensemble means is not created artificially by ensemble averaging. Importantly, SMYLE retains a larger SCF than HRDP when compared at the same ensemble size, indicating that its more dominant leading SST–TC covariance mode cannot be explained simply by its larger ensemble size (Fig. 3). One possible explanation is that SST–TC covariance in SMYLE is more strongly concentrated in a single large-scale climate mode, whereas HRDP distributes a larger fraction of its covariance across additional modes and regional processes. The lower-resolution SMYLE may therefore express TC variability more strongly through broad large-scale climate constraints, while the higher-resolution HRDP permits a richer set of dynamical pathways linking multiple modes of climate variability to TC occurrence.

The corresponding spatial patterns also converge rapidly with ensemble size. The SMYLE SST pattern is already strongly correlated with observations using a single member and changes relatively little beyond a few members, whereas HRDP exhibits a weaker but similarly stable SST-pattern correspondence (Fig. 4b; Supplementary Figs. 4,6). On the TC side, SMYLE again shows a strong observed-like regional pattern even at small ensemble sizes, while HRDP converges progressively toward the observed Gulf–Caribbean structure as additional members are averaged (Fig. 4c; Supplementary Figs. 5,7). The rapid convergence of the SVD structure with ensemble size does not imply that individual ensemble members provide equivalent TC prediction skill;

rather, it indicates that the large-scale SST–TC covariance structure is robust, while seasonal TC activity still varies substantially among individual ensemble members.

The temporal evolution of the SST component is also highly predictable. Correlations between the observed and predicted SST-side SVD1 expansion coefficients reach approximately 0.81 in HRDP and 0.84 in SMYLE using the full ensembles (Fig. 4d). Much of this skill is already present in individual realizations, with median correlations of about 0.72 in HRDP and 0.78 in SMYLE for a single member, and the correlations increase only modestly after several members are averaged. Thus, the predictable evolution of the large-scale SST state is not an artifact of extensive ensemble averaging; rather, averaging primarily suppresses realization-specific variability and more clearly isolates its systematic relationship with regional TC occurrence.

To further assess how strongly the regional prediction skill is associated with the leading coupled mode, we remove the TC-side SVD1 component from both the observed and predicted TC track-density fields and recompute the ACC (Supplementary Fig. 8). Prediction skill decreases substantially over the Gulf–Caribbean region in both HRDP and SMYLE, although appreciable residual skill remains. This indicates that a substantial portion of the common regional prediction skill is concentrated in TC variability represented by the leading SST–TC coupled mode.

These results also clarify the apparently weak model-internal TC signal diagnosed in SMYLE. S2T and SCF describe different aspects of the prediction system: S2T measures the amplitude of ensemble-coherent TC variability relative to total TC variability, whereas SCF measures how strongly the SST–TC covariance is organized into a dominant spatial mode. SMYLE can therefore exhibit a small TC S2T while simultaneously maintaining a highly organized SST–TC relationship that is evident even in individual realizations. The common Gulf–Caribbean prediction skill in HRDP and SMYLE is therefore associated with a shared, highly predictable large-scale SST pattern, despite substantial differences in the amplitude of their model-internal TC signals.

Atmospheric pathway linking predictable SST variability to regional TC occurrence

To examine how the leading SST mode modulate regional TC activity, we regress key large-scale atmospheric fields onto the standardized SST-side SVD1 expansion coefficient (Fig. 5). The resulting patterns are broadly consistent across ERA5, HRDP, and SMYLE, indicating that the predictable SST variability is accompanied by a coherent atmospheric response in both observations and prediction systems.

For the displayed phase of SVD1 associated with enhanced Gulf–Caribbean TC occurrence, all three datasets show reduced 200–850-hPa vertical wind shear extending from Central America and the Caribbean into the tropical North Atlantic, together with enhanced shear farther south over the eastern tropical Pacific and in parts of the subtropical Atlantic (Fig. 5a,c,e). The vertical-motion response provides a complementary signal. Negative 500-hPa vertical velocity anomalies extend across Central America, the Caribbean, and portions of the tropical Atlantic, while pronounced positive vertical velocity anomalies are present over the equatorial eastern Pacific (Fig. 5b,d,f). The co-occurrence of reduced vertical wind shear and enhanced ascent over the Caribbean–tropical Atlantic provides a physically consistent environment for increased TC activity. Importantly, these atmospheric anomalies are not uniformly collocated with the regions of maximum TC track-density response. In particular, the local shear and vertical velocity signals are weaker over the

northern Gulf, suggesting that the enhanced Gulf-region track density may partly reflect storms developing or surviving farther upstream before subsequently entering the region.

The deep-layer steering flow regressions further indicate a coherent circulation adjustment accompanying the SST mode (Fig. 5a,c,e). Although the detailed vector patterns differ among ERA5, HRDP, and SMYLE, all three show broad changes in the tropical and subtropical Atlantic circulation that can modulate subsequent TC propagation. We therefore interpret the leading SST pattern as influencing regional TC occurrence through a combination of changes in the environment for TC development and translation and changes in the large-scale circulation governing TC movement, rather than through a purely local response at each grid point. The broad agreement of these atmospheric responses across observations and both prediction systems provides a physical pathway linking the predictable large-scale SST variability to the common Gulf–Caribbean TC signal identified in the preceding analyses.

The agreement is particularly notable in SMYLE. Despite its climatological deficiency, likely due to its coarser atmospheric resolution (~1°), the large-scale atmospheric response associated with SVD1 closely resembles ERA5: the location and sign of the vertical-shear anomalies are well reproduced, and the vertical-motion response is even stronger in amplitude over parts of the eastern Pacific–Caribbean sector (Fig. 5e,f). Thus, SMYLE can substantially underestimate the mean TC population while still capturing the large-scale climate response that conditions year-to-year regional TC occurrence. This provides a physical basis for understanding how the lower-resolution system can retain substantial, and in parts of the Gulf–Caribbean region even higher, TC prediction skill than HRDP despite its pronounced climatological bias.

Discussion

Our results show that the regional distribution of North Atlantic TCs contains a robust seasonal prediction signal that persists after detrending, exceeds persistence, and is reproduced by two substantially different initialized prediction systems. Remarkably, comparable Gulf–Caribbean skill emerges despite large differences in simulated TC climatology and model-internal signal-to-noise characteristics. The common element is a predictable large-scale SST pattern and its associated atmospheric response, which systematically organizes regional TC occurrence.

This comparison highlights an important distinction between climatological realism and prediction of interannual variability. Higher-resolution models substantially improve the representation of TC frequency and spatial climatology (29, 30), yet this does not automatically translate into higher correlation skill for regional year-to-year variations. SMYLE strongly underestimates TC activity but nevertheless captures the large-scale atmospheric responses associated with the predictable SST mode and achieves regional skill comparable to, and locally higher than, HRDP. This result does not diminish the importance of model resolution. Realistic TC frequency, intensity and structure remain essential for predicting absolute storm numbers, major hurricanes and intensity-dependent hazards. Rather, it suggests that seasonal prediction skill also depends on whether a model correctly represents how TC occurrence responds to predictable large-scale climate variability. This interpretation is consistent with recent GFDL model comparisons showing that improved environmental prediction alone does not guarantee improved TC forecasts when the simulated TC response to that environment is biased (11).

The signal-to-noise analysis further illustrates why model-internal predictability should be interpreted carefully for intermittent weather events. The signal-to-noise paradox was highlighted prominently in seasonal predictions of the NAO, where high forecast–observation correlations coexist with a relatively weak predictable signal within individual model realizations (23, 31, 32). Large ensembles can recover this weak signal by suppressing realization-specific atmospheric variability. Regional TC occurrence presents a related but physically distinct situation. TCs are discrete and highly intermittent events, so individual ensemble members can contain very different genesis events and tracks even when they experience similar large-scale environmental conditions. Consequently, a weak ensemble-coherent TC signal does not necessarily imply that regional TC activity conditioned by large-scale climate variability is poorly predictable.

This distinction is particularly apparent in SMYLE. Its weak S2T and RPC substantially above one coexists with robust Gulf–Caribbean skill, whereas HRDP exhibits a stronger ensemble-coherent signal and RPC closer to unity without corresponding higher observed skill. Moreover, the leading SST–TC relationship is already evident at the single-member level. Its SCF is comparable to observations, and its spatial structure resembles the observed mode, while the temporal evolution of the associated SST variability is highly predictable, with full-ensemble ACCs exceeding 0.8 in both systems. Ensemble averaging strengthens this organization but does not create it. Thus, model S2T describes how clearly a predictable response emerges relative to ensemble variability within a particular model, but it does not by itself determine prediction skill against observations.

More broadly, our results suggest that highly intermittent extreme weather can remain seasonally predictable when its occurrence is systematically modulated by predictable large-scale climate variability, rather than requiring strong agreement among individual ensemble members. A lower-resolution model may therefore retain useful seasonal prediction skill even when its ensemble coherence is weak, provided that it captures how large-scale climate variability modulates regional event occurrence. This perspective may extend beyond TCs to other intermittent extreme-weather phenomena, including mesoscale convective systems (MCSs) (38) and other severe convective storms.

Several limitations and directions for future work remain. The present study focuses on seasonal prediction of NA TC activity, while seasonal prediction skill over the Pacific and, more broadly, multiyear TC prediction skills are beyond the scope of the present study and will be examined in a separate study. The leading SST pattern contains substantial variability in both the tropical Pacific and NA, and the relative roles of Pacific and Atlantic SST variability in generating the regional TC response cannot be uniquely separated here. Targeted SST perturbation experiments would help quantify their individual and combined contributions. TC track density also integrates genesis, development and propagation, which should be decomposed in future work, particularly given the weaker local atmospheric response over the northern Gulf. Nevertheless, their agreement points to a common large-scale physical constraint on regional TC occurrence and provides a framework for understanding how meaningful seasonal prediction skill can emerge even when individual extreme-weather realizations remain highly variable.

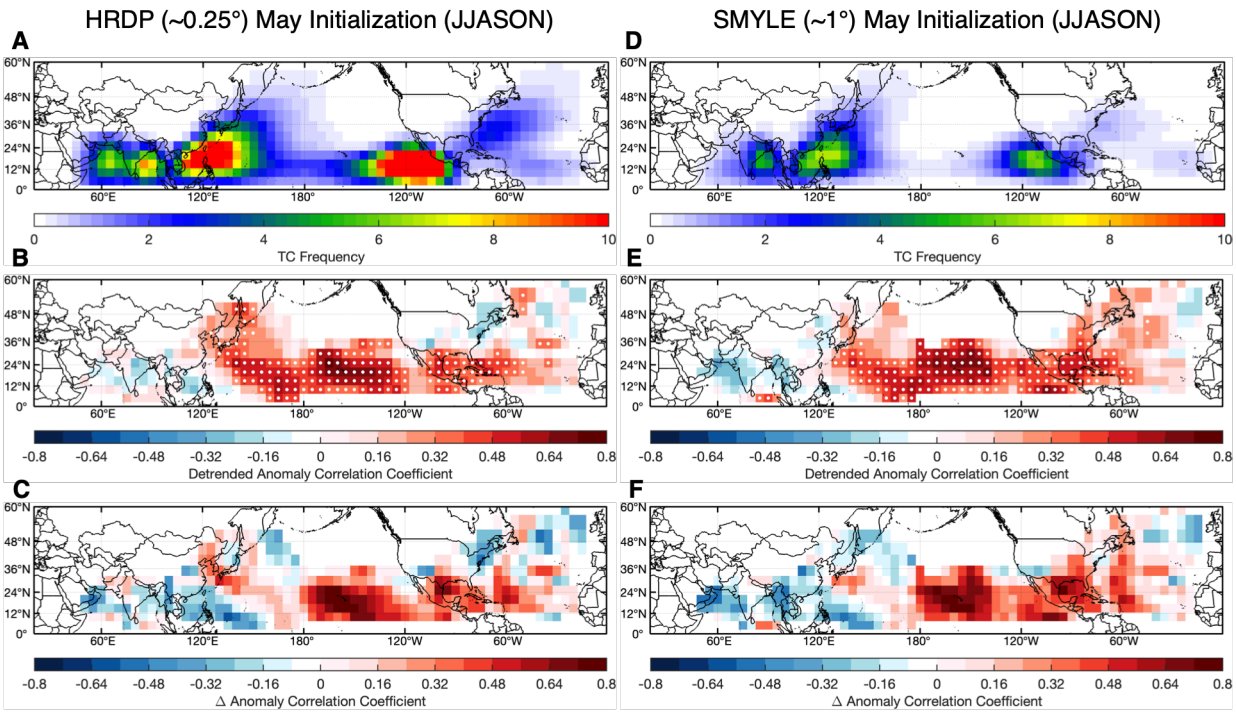


Figure 1. TC track density climatology and seasonal prediction skill in HRDP and SMYLE. (**A**) Climatological June–November (JJASON) TC track density from the 10-member ensemble mean May-initialized HRDP hindcasts over 1980–2023. (**B**) Detrended anomaly correlation coefficients (ACCs) between observed and ensemble mean JJASON TC track density in HRDP. Linear trends are removed separately from the observed and predicted time series at each grid point before calculating the ACC. White stippling denotes correlations statistically significant at the 95% confidence level. (**C**) Difference between the detrended ACC of the initialized HRDP forecasts and that of the persistence forecast. Persistence prediction is based on trailing 5-year averages. (**D**–**F**) As in (**A**–**C**), but for the 20-member ensemble SMYLE hindcasts.

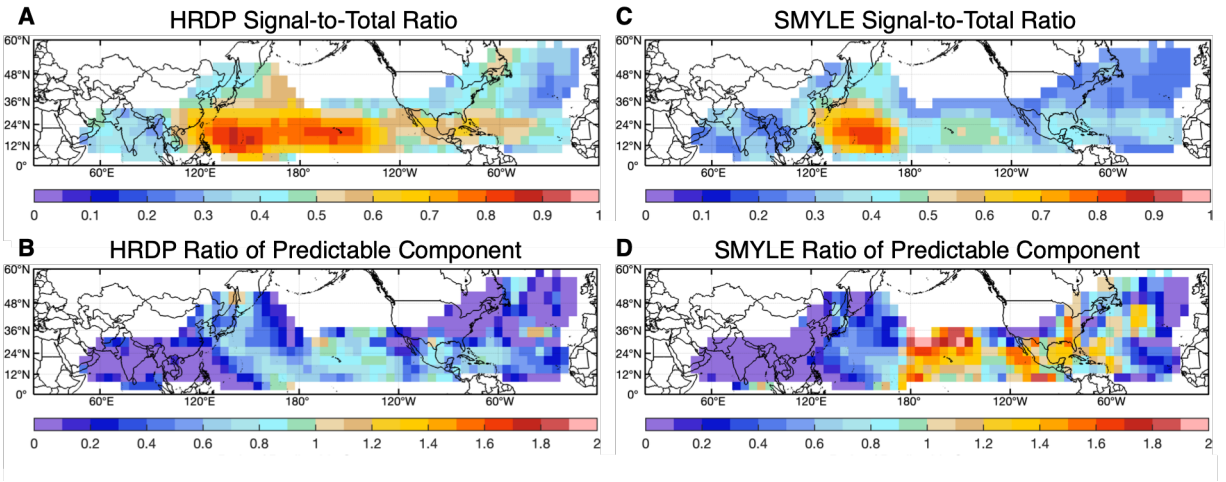


Figure 2. Model signal-to-noise characteristics of seasonal TC track density predictions in HRDP and SMYLE. (**A**) Signal-to-total ratio (S2T) of JJASON TC track density in the May-initialized HRDP hindcasts over 1980–2023. S2T measures the amplitude of the ensemble-mean predictable signal relative to the total year-to-year variability represented by the ensemble (see Methods). (**B**) Ratio of predictable components (RPC) for HRDP, defined as the detrended ACC divided by S2T. RPC values greater than one indicate that the forecast–observation correlation is larger than expected from the model-internal predictable signal, whereas values below one indicates the opposite. (**C,D**) As in (**A,B**), but for the SMYLE hindcasts.

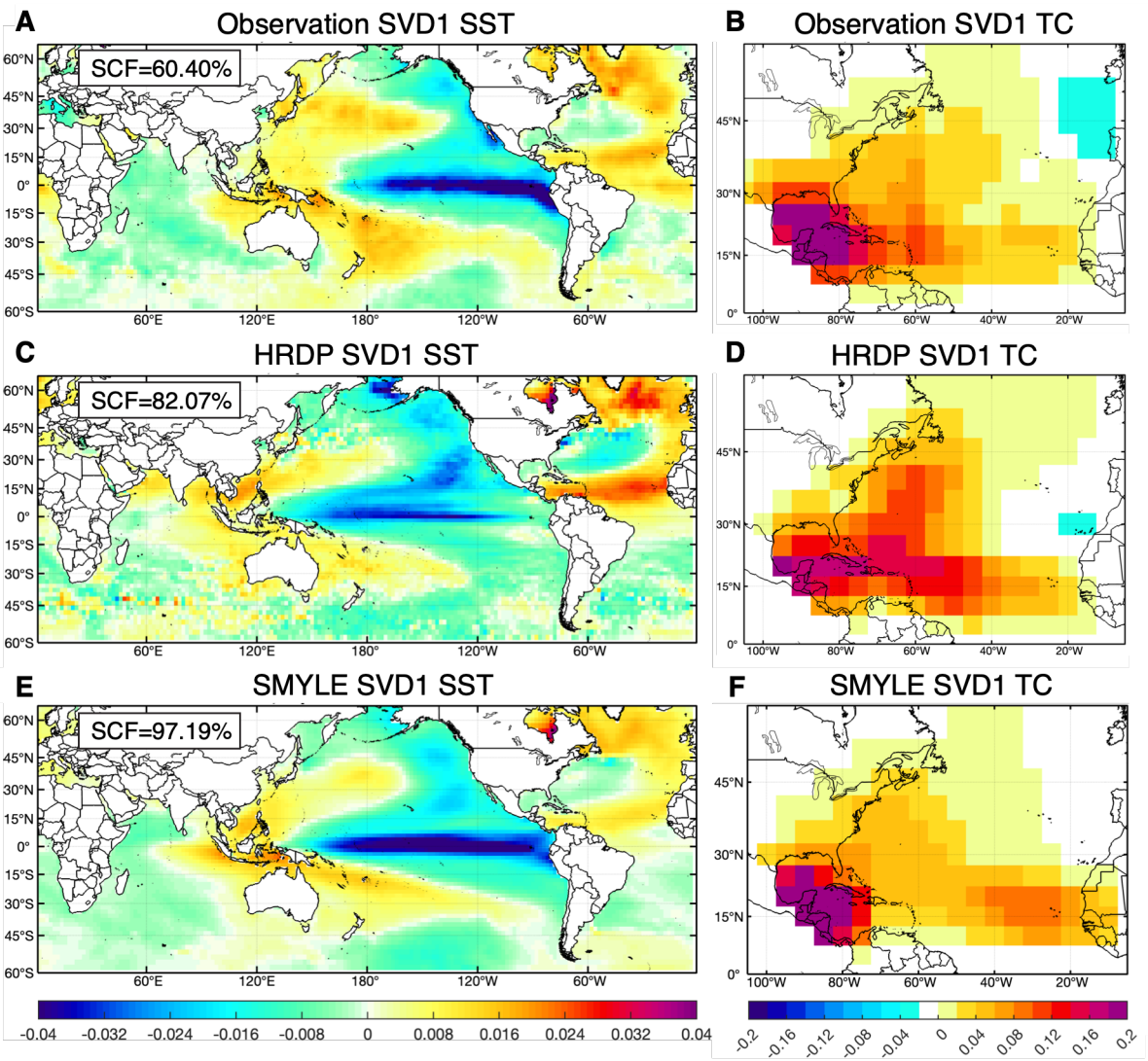


Figure 3. Leading coupled modes between JJASON global SST and North Atlantic TC track density. Observed SVD1 (**A**) SST pattern and corresponding (**B**) TC track density pattern. (**C,D**) As in (**A,B**), but for the 10-member ensemble mean HRDP hindcasts. (e,f) As in (a,b), but for the 20-member ensemble-mean SMYLE hindcasts. The squared covariance fraction (SCF) explained by SVD1 is annotated in the SST panels. The higher SCF in HRDP and SMYLE partly reflects the use of ensemble means, which suppress internal variability and more clearly isolate the ensemble-coherent SST–TC covariance structure.

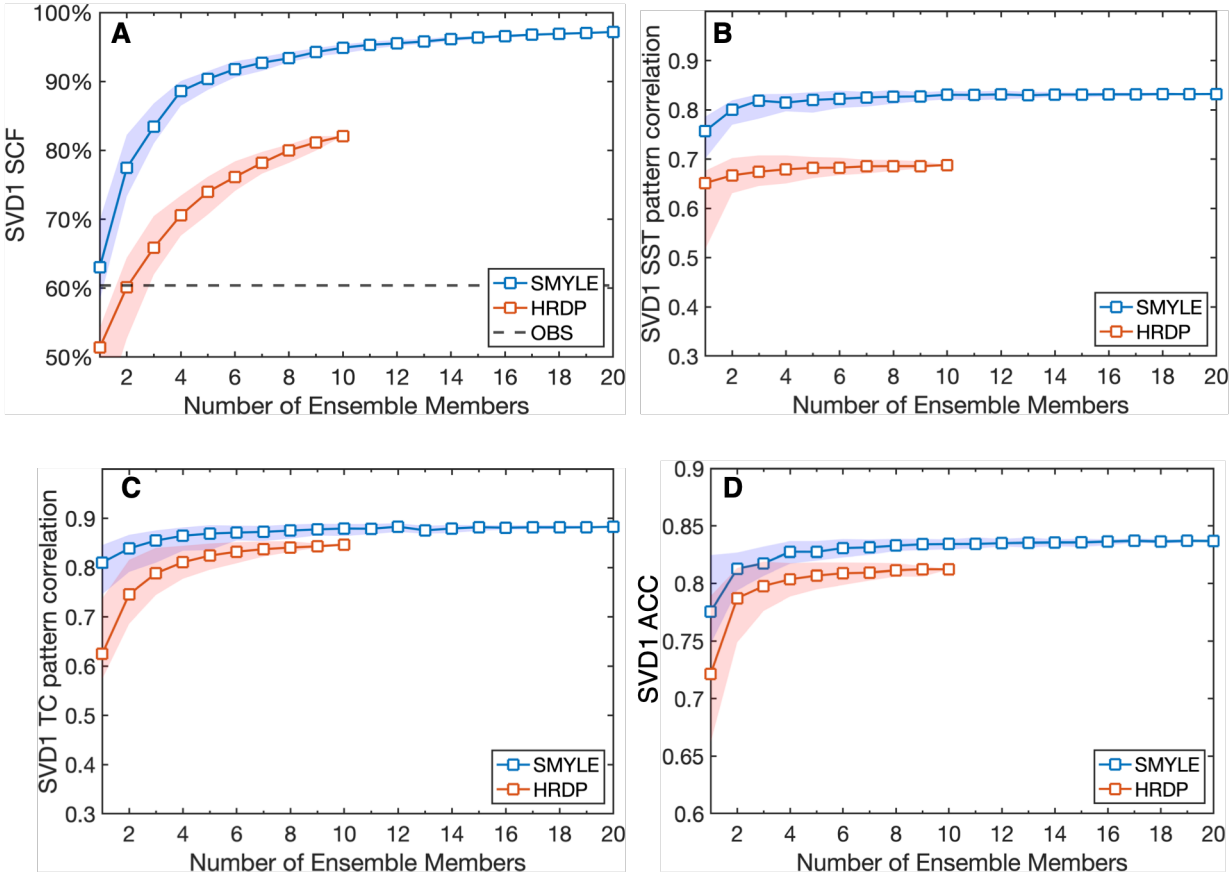


Figure 4. Ensemble-size dependence of the leading SST–TC covariance mode and its prediction skill. For each ensemble size, HRDP (red) and SMYLE (blue) members are subsampled without replacement, the selected members are averaged, and SVD analysis is performed between the ensemble-mean SST and the NA TC track density fields (Methods). Curves show the median across the subsamples; shading indicates the interquartile ranges among subsamples. (**A**) Squared covariance fraction (SCF) explained by SVD1. The dashed line denotes the observed SCF (60.4%). (**B**) Spatial correlation between the modeled and observed SVD1 SST patterns. (**C**) Spatial correlation between the modeled and observed SVD1 TC track density patterns. (**D**) Temporal anomaly correlation coefficient (ACC) between the modeled and observed SST-side SVD1 expansion coefficients.

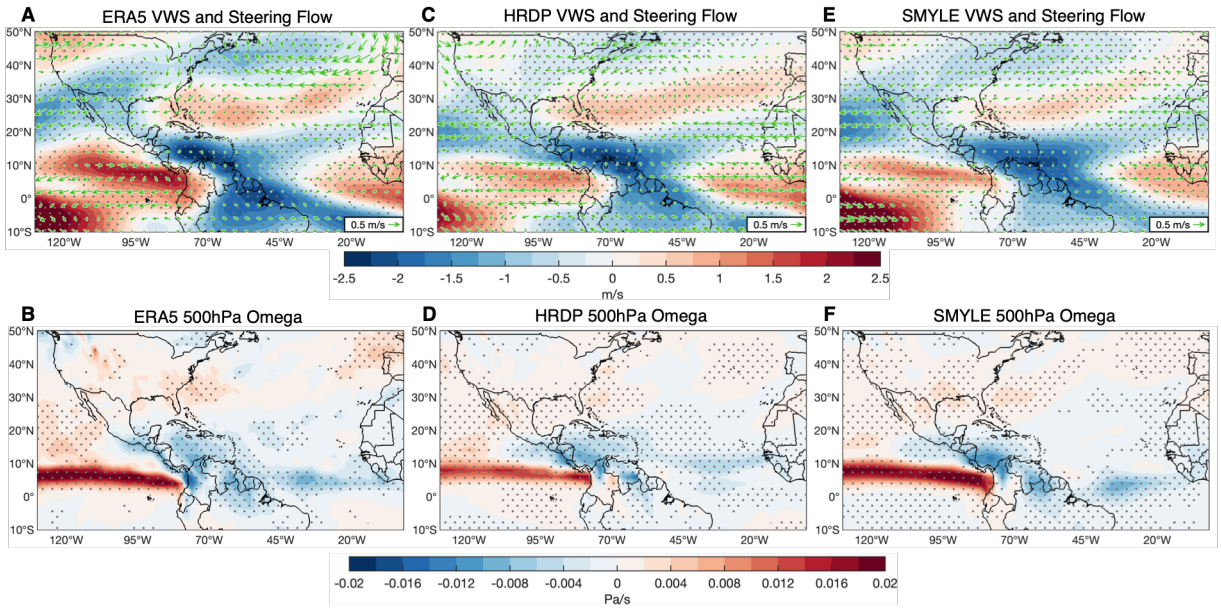


Figure 5. Atmospheric responses associated with the leading SST–TC covariance mode. (**A**) Regression of 200–850-hPa vertical wind shear (shading) and 300-800hPa mass-weighted TC steering flow (vectors) onto the standardized SST-side SVD1 expansion coefficient in ERA5. (**B**) As in (**A**), but for 500-hPa vertical pressure velocity. Negative values indicate anomalous ascent, and positive values indicate anomalous subsidence. (**C,D**) As in (**A,B**), but for HRDP. (**E,F**) As in (**A,B**), but for SMYLE. Stippling denotes regression anomalies statistically significant at the 90% confidence level.

Methods

High-Resolution Decadal Prediction

The HRDP system is based on the high-resolution configuration of the Community Earth System Model version 1.3 (CESM1.3) (25–27). HRDP uses approximately 0.25° horizontal resolution in the atmosphere and land components and 0.1° resolution in the ocean and sea-ice components. The atmospheric component uses the spectral-element dynamical core version of the Community Atmosphere Model version 5 (CAM5-SE) with 30 vertical levels, while the land component uses the Community Land Model version 4 (CLM4). The ocean component is the Parallel Ocean Program version 2 (POP2) with 62 vertical levels, and the sea-ice component is the Community Ice Code version 4 (CICE4). This configuration is eddy rich in the ocean and permits substantially improved representation of TCs relative to conventional ~1° climate models (25).

HRDP employs full-field initialization of all model components. Ocean and sea-ice initial conditions are obtained from a high-resolution forced ocean–sea-ice simulation (HR-FOSI) using the same 0.1° ocean and sea-ice models as HRDP and surface forcing based on the Japanese 55-year Reanalysis (JRA55-do) (39) following the OMIP2 protocol. Atmospheric initial conditions are obtained by regridding fields from the JRA55, while land initial conditions are taken from a high-resolution atmosphere–land simulation forced by observed SSTs as part of the CESM1.3 HighResMIP simulations (40). Ensemble members are generated using round-off-level perturbations to the atmospheric potential-temperature initial conditions.

The expanded HRDP prediction archive consists of 10-member, 62-month initialized predictions with May and November start dates for each year. In this study, we use the 44 annual May-initialized 10-member hindcasts from 1980–2023 and analyze TC activity during the subsequent June–November (JJASON) hurricane season. Thus, all HRDP prediction statistics are based on the ensemble mean of the 10 members unless otherwise noted. The expanded May- and November-initialized HRDP archive extends the original HRDP hindcast (27), which was based on every other year November initializations between 1976 and 2016.

Seasonal to Multiyear Large Ensemble

The SMYLE system is based on the CESM version 2 (CESM2) (28, 41) configured at nominal 1° horizontal resolution across the coupled system. The atmospheric component uses the finite-volume dynamical core version of CAM version 6 (CAM6-FV) with 32 vertical levels, the ocean component is the POP2 with 60 vertical levels, the sea-ice component is CICE5, and the land component is CLM5. SMYLE consists of 20-member, 24-month initialized predictions with four initialization dates each year on 1 February, 1 May, 1 August, and 1 November (28). In this study, we use the 20-member May-initialized SMYLE predictions from 1980–2023 and analyze TC activity during the subsequent JJASON season, consistent with the HRDP analysis. Unless otherwise noted, SMYLE prediction statistics are calculated from the 20-member ensemble.

As in HRDP, SMYLE employs full-field initialization of all model components, although the initialization configurations differ in several respects (Supplementary Table 1). Atmospheric initial conditions are obtained by interpolating JRA-55 fields onto the CAM6-FV grid. Ocean and sea-ice initial conditions are obtained from a CESM2 forced ocean–sea-ice simulation (FOSI) driven by JRA55-do atmospheric forcing following the OMIP2 framework, conceptually similar to HR-FOSI but using the nominal 1° POP2 configuration. Land initial conditions are obtained from a forced CLM5 simulation using CRU-JRAv2 atmospheric forcing.

Although CESM1.3 HRDP and CESM2 SMYLE both belong to the CESM family, they represent substantially different prediction-system configurations. They are based on different

CESM generations and differ in horizontal resolution, atmospheric dynamical cores, physical parameterizations, and component-model configurations. These structural differences make their agreement particularly useful for assessing the robustness of regional TC predictability and whether its associated physical sources are consistently represented across distinct climate prediction systems. The comparison is therefore intended primarily to assess the consistency of regional TC predictability and its physical sources across the two systems, rather than to isolate the effects of any individual model configuration difference.

Tropical cyclone detection and track density

We use 6-hourly model output to detect and track TCs. For HRDP, TC detection and tracking are performed using the TempestExtremes algorithm (42), following the criteria used in previous studies (21, 43). TC candidates are initially identified as local minima in sea level pressure (SLP), with a closed-contour criterion requiring an increase of at least 5 hPa within 5.5° of the candidate nodes. A warm-core criterion is additionally imposed, requiring the 250–500-hPa geopotential height difference to decrease by at least 8 m within 6.5° of the candidates and the corresponding maximum geopotential height anomaly to occur within 1° of the candidate centers. Candidate nodes are then stitched in time to form storm tracks. Detected storms are required to have a minimum lifetime travel distance of 8° great circle distance, a minimum duration of 2.5 days, and a lifetime maximum surface wind speed exceeding 17.5 m/s (34 kt; tropical storm intensity). TCs are further required to form between 5° and 40° latitude.

For SMYLE, we similarly apply TempestExtremes but use relaxed detection thresholds to account for its coarser atmospheric resolution (28). The closed-contour criterion requires an SLP increase of at least 2 hPa within 5.5° of the candidate nodes, while the warm-core criterion requires the 250–500-hPa geopotential height difference to decrease by at least 4 m within 6.5° of the candidates. All subsequent tracking and filtering criteria are kept consistent with HRDP, including a minimum lifetime travel distance of 8°, a minimum duration of 2.5 days, a lifetime maximum surface wind speed exceeding 17.5 m/s, and genesis between 5° and 40° latitude. The relaxed detection thresholds in SMYLE are intended to account for the weaker representation of TC structure at nominal 1° atmospheric resolution while retaining consistent lifetime and intensity requirements across the two prediction systems.

TC track density is defined as the number of 6-hourly TC track positions passing through each 5° × 5° grid box in each JJASON hurricane season, thereby accounting for both TC genesis locations and subsequent storm trajectories. Following previous studies (20, 44), the resulting track-density fields are spatially smoothed using a nine-point moving average, with weights determined by distance from the center of each grid box.

Observed data

For the observed TC activity, we used the International Best Track Archive for Climate Stewardship (IBTrACS) (45) version 4, for the period 1980 to 2023. IBTrACS compiles best-track records from multiple operational agencies. In this study, we used the agency-consistent records identified by the "USA Agency" flag, which combines best-track information from the National Hurricane Center, Joint Typhoon Warning Center, and Central Pacific Hurricane Center over the Northern Hemisphere.

Observed SST was obtained from the UK Met Office Hadley Centre Sea Ice and Sea Surface Temperature dataset (HadISST1.1) (46). Large-scale atmospheric circulation fields were obtained

from the ERA5 reanalysis (47) and were used to characterize the large-scale atmospheric circulations and calculate the mass-weighted TC steering flow.

Skill metrics

Prediction skill is evaluated using the anomaly correlation coefficient (ACC), signal-to-total ratio (S2T), and ratio of predictable components (RPC), following previous studies (23 and 27). All metrics are calculated at each grid point using June-November (JJASON) tropical cyclone track density over 1980-2023. Forecast and observed time series are converted to anomalies relative to their respective 1980-2023 climatology. Linear trends are removed separately from the forecast and observed anomaly time series before calculating the skill metrics.

Let f'_{im} denote the linearly detrended forecast anomaly for initialization year i and ensemble member m, and o'_i the corresponding detrended observed anomaly. Here, $N = 44$ is the number of hindcast years and M is the number of ensemble members ($M = 10$ for HRDP and $M = 20$ for SMYLE). The ensemble-mean forecast anomaly is

$$\bar{f}'_i = \frac{1}{M}\sum_{m=1}^{M} f'_{im}.$$

The ACC measures the linear association between the ensemble-mean forecast and observations and is calculated as

$$\mathrm{ACC} = \frac{\sum_{i=1}^{N} \bar{f}'_i o'_i}{\sqrt{\left(\sum_{i=1}^{N} (\bar{f}'_i)^2\right)\left(\sum_{i=1}^{N} (o'_i)^2\right)}}.$$

ACC primarily measures the correct phasing of interannual variability and is insensitive to differences in anomaly amplitude.

The model-internal predictable signal is quantified using the signal-to-total ratio,

$$\mathrm{S2T} = \frac{\sigma^f_{\mathrm{sig}}}{\sigma^f_{\mathrm{tot}}},$$

where the signal variability is estimated from the temporal variability of the ensemble mean,

$$\sigma^f_{\mathrm{sig}} = \sqrt{\frac{1}{N}\sum_{i=1}^{N}\left(\frac{1}{M}\sum_{m=1}^{M} f'_{im}\right)^2},$$

and the total variability is estimated from individual-member time series,

$$\sigma^f_{\mathrm{tot}} = \sqrt{\frac{1}{K}\sum_{k=1}^{K}\left[\frac{1}{N}\sum_{i=1}^{N}\left(f'_{i\,m_{ki}}\right)^2\right]}.$$

Following previous study (27), σ^f_{tot} is estimated using $K = 100$ Monte Carlo realizations. For each realization k, one ensemble member m_{ki} is randomly selected for each initialization year i. S2T therefore measures the amplitude of ensemble-coherent interannual variability relative to the total variability represented by individual ensemble members. Larger S2T indicates a stronger model-internal predictable signal.

The ratio of predictable components is defined as

$$\mathrm{RPC} = \frac{\mathrm{ACC}}{\sigma_{\mathrm{sig}}^{f}/\sigma_{\mathrm{tot}}^{f}} = \frac{\mathrm{ACC}}{\mathrm{S2T}}.$$

RPC compares observed prediction skill with the amplitude of the model-internal predictable signal. An RPC near one indicates broad consistency between model-internal predictability and forecast-observation skill. RPC values greater than one indicate that forecast-observation correlation is larger than expected from the model-internal predictable signal, corresponding to an underconfident prediction system or signal-to-noise paradox, whereas values below one indicates the overconfident (48). Following previous study (27), RPC is set to zero where ACC is negative. Because ACC provides only a lower-bound estimate of the predictable component of the real world, RPC should be interpreted cautiously where ACC is small.

SVD analysis

Following the previous study (49), we applied singular value decomposition (SVD) to identify the dominant coupled modes of variability between seasonal SSTs and TC activity. SVD is commonly used in climate studies to characterize spatial patterns in two fields that maximize their squared covariance and thereby isolate the dominant modes of covariability between them. SST is analyzed on a 2° × 2° grid over the global domain, whereas TC track density is analyzed on the 5° × 5° grid described above over the North Atlantic domain. Prior to the SVD analysis, linear trends are removed from both the SST and TC track-density fields at each grid point.

A cross-covariance matrix is then constructed between the SST and TC anomaly fields and decomposed using SVD. The decomposition produces paired SST and TC spatial patterns for each mode, together with a singular value that measures the covariance captured by that mode. The fraction of total squared covariance (SCF) explained by each mode is quantified as

$$SCF_i = \frac{{\sigma_i}^2}{\sum {\sigma_j}^2}$$

where σ_i is the singular value associated with mode i. We focus primarily on the leading mode, SVD1, which represents the dominant large-scale SST pattern covarying with North Atlantic TC track density variability.

The temporal evolution of each SVD mode is characterized by expansion coefficients obtained by projecting the SST and TC anomaly fields onto their corresponding SVD spatial patterns. These expansion coefficients describe the year-to-year amplitude of the coupled mode and are used to assess the temporal correspondence between observations and initialized predictions. Because the sign of an SVD mode is mathematically arbitrary, the signs of the paired SST and TC patterns are oriented consistently across observations and prediction systems to facilitate comparison.

SVD is performed separately for observations, the HRDP ensemble mean, and the SMYLE ensemble mean. To examine the sensitivity of the leading SST–TC covariance structure to ensemble size, we additionally repeat the SVD analysis using subsets of ensemble members. For each ensemble size, members are sampled without replacement and averaged to construct ensemble-mean SST and TC track density fields, after which the SVD analysis is repeated. When the number of possible member combinations exceeds 1,000, we randomly select 1,000 unique combinations; otherwise, all possible combinations are used. For each subset, we record the SVD1 SCF, the spatial correlations of the SST-side and TC-side SVD1 patterns with the corresponding observed patterns, and the temporal ACC between the modeled and observed SST-side SVD1 expansion coefficients. Mode signs are aligned before calculating pattern and temporal

correlations. Figure 4 shows the median across member subsets, with shading indicating the interquartile range.

To diagnose the large-scale atmospheric circulation associated with the leading coupled mode, we further regress seasonal anomalies of 200–850-hPa vertical wind shear, 300–800-hPa mass-weighted TC steering flow, and 500-hPa vertical pressure velocity onto the standardized SST-side SVD1 expansion coefficient (Fig. 5). The regressions are performed separately for ERA5, HRDP, and SMYLE to assess whether the atmospheric circulation associated with the observed leading SST mode is consistently represented by the two prediction systems.

Data and material availability

ECMWF ERA5 reanalysis data on single level can be accessed from the Copernicus Climate Data Store at https://cds.climate.copernicus.eu/datasets/reanalysis-era5-single-levels?tab=overview. HadISST is available from https://www.metoffice.gov.uk/hadobs/hadisst/index.html. IBTrACS tropical cyclone data is obtained from https://www.ncei.noaa.gov/products/international-best-track-archive. The CESM2 SMYLE are available through the NSF NCAR Geoscience Data Exchange (GDEX) platform at https://gdex.ucar.edu/datasets/d651065/. The CESM1.3 code used to generate HRDP is available at https://github.com/ihesp/cesm/tree/ihesp-hires-master. The complete HRDP archive is being prepared for release through GDEX.

References and Notes

1. Klotzbach, P. J., Blake, E., Camp, J., Caron, L.-P., Chan, J. C. L., Kang, N.-Y., Kuleshov, Y., Lee, S.-M., Murakami, H., Saunders, M., Takaya, Y., Vitart, F., & Zhan, R. (2019). Seasonal tropical cyclone forecasting. Tropical Cyclone Research and Review, 8(3), 134-149. https://doi.org/10.1016/j.tcrr.2019.10.003

2. Takaya, Y., Caron, L.-P., Blake, E., Bonnardot, F., Bruneau, N., Camp, J., Chan, J., Gregory, P., Jones, J. J., Kang, N., Klotzbach, P. J., Kuleshov, Y., Leroux, M.-D., Lockwood, J. F., Murakami, H., Nishimura, A., Pattanaik, D. R., Philp, T. J., Ruprich-Robert, Y., ... Zhan, R. (2023). Recent advances in seasonal and multi-annual tropical cyclone forecasting. Tropical Cyclone Research and Review, 12(3), 182-199. https://doi.org/10.1016/j.tcrr.2023.09.003

3. Charney, J. G., & Shukla, J. (1981). Predictability of monsoons. In J. Lighthill & R. P. Pearce (Eds.), Monsoon dynamics (pp. 99-110). Cambridge University Press. https://doi.org/10.1017/CBO9780511897580.009

4. Gray, W. M. (1984a). Atlantic seasonal hurricane frequency. Part I: El Niño and 30 mb quasi-biennial oscillation influences. Monthly Weather Review, 112(9), 1649-1668. https://doi.org/10.1175/1520-0493(1984)112<1649:ASHFPI>2.0.CO;2

5. Gray, W. M. (1984b). Atlantic seasonal hurricane frequency. Part II: Forecasting its variability. Monthly Weather Review, 112(9), 1669-1683. https://doi.org/10.1175/1520-0493(1984)112<1669:ASHFPI>2.0.CO;2

6. Vitart, F., & Stockdale, T. N. (2001). Seasonal forecasting of tropical storms using coupled GCM integrations. Monthly Weather Review, 129(10), 2521-2537. https://doi.org/10.1175/1520-0493(2001)129<2521:SFOTSU>2.0.CO;2

7. Vitart, F., Huddleston, M. R., Déqué, M., Peake, D., Palmer, T. N., Stockdale, T. N., Davey, M. K., Ineson, S., & Weisheimer, A. (2007). Dynamically based seasonal forecasts of Atlantic tropical storm activity issued in June by EUROSIP. Geophysical Research Letters, 34, L16815. https://doi.org/10.1029/2007GL030740

8. Camp, J., Roberts, M., MacLachlan, C., Wallace, E., Hermanson, L., Brookshaw, A., Arribas, A., & Scaife, A. A. (2015). Seasonal forecasting of tropical storms using the Met Office GloSea5 seasonal forecast system. Quarterly Journal of the Royal Meteorological Society, 141(691), 2206-2219. https://doi.org/10.1002/qj.2516

9. Murakami, H., Vecchi, G. A., Underwood, S., Delworth, T. L., Wittenberg, A. T., Anderson, W. G., ... & Zeng, F. (2015). Simulation and prediction of category 4 and 5 hurricanes in the high-resolution GFDL HiFLOR coupled climate model. Journal of Climate, 28(23), 9058-9079. https://doi.org/10.1175/JCLI-D-15-0216.1

10. Murakami, H., Vecchi, G. A., Villarini, G., Delworth, T. L., Gudgel, R., Underwood, S., Yang, X., Zhang, W., & Lin, S.-J. (2016). Seasonal forecasts of major hurricanes and landfalling tropical cyclones using a high-resolution GFDL coupled climate model. Journal of Climate, 29(22), 7977-7989. https://doi.org/10.1175/JCLI-D-16-0233.1

11. Murakami, H., Delworth, T. L., Johnson, N. C., Lu, F., McHugh, C. E., & Jia, L. (2025). Seasonal forecasts of tropical cyclones using GFDL SPEAR and HiFLOR-S. Journal of Climate, 38(9), 2015-2030. https://doi.org/10.1175/JCLI-D-24-0356.1

12. Saunders, M. A., & Lea, A. S. (2005). Seasonal prediction of hurricane activity reaching the coast of the United States. Nature, 434(7036), 1005-1008. https://doi.org/10.1038/nature03454

13. Xie, L., Yan, T., Pietrafesa, L. J., Morrison, J. M., & Karl, T. (2005). Climatology and interannual variability of North Atlantic hurricane tracks. Journal of Climate, 18(24), 5370-5381. https://doi.org/10.1175/JCLI3560.1

14. Mei, W., Xie, S.-P., & Zhao, M. (2014). Variability of tropical cyclone track density in the North Atlantic: Observations and high-resolution simulations. Journal of Climate, 27(13), 4797-4814. https://doi.org/10.1175/JCLI-D-13-00587.1

15. Vecchi, G. A., Delworth, T., Gudgel, R., Kapnick, S., Rosati, A., Wittenberg, A. T., Zeng, F., Anderson, W., Balaji, V., Dixon, K., Jia, L., Kim, H.-S., Krishnamurthy, L., Msadek, R., Stern, W. F., Underwood, S. D., Villarini, G., Yang, X., & Zhang, S. (2014). On the seasonal forecasting of regional tropical cyclone activity. Journal of Climate, 27(21), 7994-8016. https://doi.org/10.1175/JCLI-D-14-00158.1

16. Manganello, J. V., Cash, B. A., Hodges, K. I., & Kinter, J. L., III. (2019). Seasonal forecasts of North Atlantic tropical cyclone activity in the North American Multi-Model Ensemble. Climate Dynamics, 53, 7169-7184. https://doi.org/10.1007/s00382-017-3670-5

17. Befort, D. J., Hodges, K. I., & Weisheimer, A. (2022). Seasonal prediction of tropical cyclones over the North Atlantic and western North Pacific. Journal of Climate, 35(5), 1385-1397. https://doi.org/10.1175/JCLI-D-21-0041.1
18. Vimont, D. J., & Kossin, J. P. (2007). The Atlantic meridional mode and hurricane activity. Geophysical Research Letters, 34(7), L07709. https://doi.org/10.1029/2007GL029683
19. Patricola-DiRosario, C. M., Saravanan, R., & Chang, P. (2014). The impact of the El Niño-Southern Oscillation and Atlantic meridional mode on seasonal Atlantic tropical cyclone activity. Journal of Climate, 27(14), 5311-5328. https://doi.org/10.1175/JCLI-D-13-00687.1
20. Fu, D., Chang, P., Patricola-DiRosario, C. M., & Saravanan, R. (2019). High-resolution tropical channel model simulations of tropical cyclone climatology and intraseasonal-to-interannual variability. Journal of Climate, 32(22), 7871-7895. https://doi.org/10.1175/JCLI-D-19-0130.1
21. Zhang, Q., Chang, P., Fu, D., Yeager, S. G., Danabasoglu, G., Castruccio, F., & Rosenbloom, N. (2024). Enhanced Atlantic Meridional Mode predictability in a high-resolution prediction system. Science Advances, 10(31), eado6298. https://doi.org/10.1126/sciadv.ado6298
22. Doane-Solomon, R., Befort, D. J., Camp, J., Hodges, K., & Weisheimer, A. (2024). The link between North Atlantic tropical cyclones and ENSO in seasonal forecasts. Atmospheric Science Letters, 25(1), e1190. https://doi.org/10.1002/asl.1190
23. Eade, R., Smith, D., Scaife, A., Wallace, E., Dunstone, N., Hermanson, L., & Robinson, N. (2014). Do seasonal-to-decadal climate predictions underestimate the predictability of the real world? Geophysical Research Letters, 41(15), 5620-5628. https://doi.org/10.1002/2014GL061146
24. Zhang, G., Murakami, H., Gudgel, R., & Yang, X. (2019). Dynamical seasonal prediction of tropical cyclone activity: Robust assessment of prediction skill and predictability. Geophysical Research Letters, 46(10), 5506-5515. https://doi.org/10.1029/2019GL082529
25. Chang, P., Zhang, S., Danabasoglu, G., Yeager, S. G., Fu, H., Wang, H., ... & Wu, L. (2020). An unprecedented set of high-resolution Earth system simulations for understanding multiscale interactions in climate variability and change. Journal of Advances in Modeling Earth Systems, 12(12), e2020MS002298. https://doi.org/10.1029/2020MS002298
26. Chang, P., Fu, D., Liu, X., Castruccio, F. S., Prein, A. F., Danabasoglu, G., ... & Bates, S. C. (2026). Future extreme precipitation amplified by intensified mesoscale moisture convergence. Nature Geoscience, 19(1), 33-41. https://doi.org/10.1038/s41561-025-01859-1
27. Yeager, S. G., Chang, P., Danabasoglu, G., Rosenbloom, N., Zhang, Q., Castruccio, F. S., Gopal, A., Rencurrel, M. C., & Simpson, I. R. (2023). Reduced Southern Ocean warming enhances global skill and signal-to-noise in an eddy-resolving decadal prediction system. npj Climate and Atmospheric Science, 6, 107. https://doi.org/10.1038/s41612-023-00434-y
28. Yeager, S. G., Rosenbloom, N., Glanville, A. A., Wu, X., Simpson, I., Li, H., Molina, M. J., Krumhardt, K., Mogen, S., Lindsay, K., Lombardozzi, D., Wieder, W., Kim, W. M., Richter, J. H., Long, M., Danabasoglu, G., Bailey, D., Holland, M., Lovenduski, N., ... King, T.

(2022). The Seasonal-to-Multiyear Large Ensemble (SMYLE) prediction system using the Community Earth System Model version 2. Geoscientific Model Development, 15, 6451-6493. https://doi.org/10.5194/gmd-15-6451-2022

29. Roberts, M. J., Camp, J., Seddon, J., Vidale, P. L., Hodges, K., Vanniere, B., ... & Ullrich, P. (2020a). Impact of model resolution on tropical cyclone simulation using the HighResMIP-PRIMAVERA multimodel ensemble. Journal of Climate, 33(7), 2557-2583. https://doi.org/10.1175/JCLI-D-19-0639.1
30. Roberts, M. J., Camp, J., Seddon, J., Vidale, P. L., Hodges, K., Vannière, B., ... & Wu, L. (2020b). Projected future changes in tropical cyclones using the CMIP6 HighResMIP multimodel ensemble. Geophysical Research Letters, 47(14), e2020GL088662. https://doi.org/10.1029/2020GL088662
31. Scaife, A. A., Arribas, A., Blockley, E., Brookshaw, A., Clark, R. T., Dunstone, N., ... & Williams, A. (2014). Skillful long-range prediction of European and North American winters. Geophysical Research Letters, 41(7), 2514-2519. https://doi.org/10.1002/2014GL059637
32. Dunstone, N., Smith, D., Scaife, A., Hermanson, L., Eade, R., Robinson, N., ... & Knight, J. (2016). Skilful predictions of the winter North Atlantic Oscillation one year ahead. Nature Geoscience, 9(11), 809-814. https://doi.org/10.1038/ngeo2824
33. Scaife, A. A., & Smith, D. (2018). A signal-to-noise paradox in climate science. npj Climate and Atmospheric Science, 1, 28. https://doi.org/10.1038/s41612-018-0038-4
34. Smith, D. M., Scaife, A. A., Eade, R., Athanasiadis, P., Bellucci, A., Bethke, I., ... & Zhang, L. (2020). North Atlantic climate far more predictable than models imply. Nature, 583(7818), 796-800. https://doi.org/10.1038/s41586-020-2525-0
35. Marshall, J., Kushnir, Y., Battisti, D., Chang, P., Czaja, A., Dickson, R., Hurrell, J., McCartney, M., Saravanan, R., & Visbeck, M. (2001). North Atlantic climate variability: Phenomena, impacts and mechanisms. International Journal of Climatology, 21(15), 1863-1898. https://doi.org/10.1002/joc.693
36. Czaja, A., & Frankignoul, C. (2002). Observed impact of Atlantic SST anomalies on the North Atlantic Oscillation. Journal of Climate, 15(6), 606-623. https://doi.org/10.1175/1520-0442(2002)015<0606:OIOASA>2.0.CO;2
37. Hurrell, J. W., Kushnir, Y., Ottersen, G., & Visbeck, M. (2003). An overview of the North Atlantic Oscillation. In J. W. Hurrell, Y. Kushnir, G. Ottersen, & M. Visbeck (Eds.), The North Atlantic Oscillation: Climatic significance and environmental impact (Geophysical Monograph Series, Vol. 134). American Geophysical Union. https://doi.org/10.1029/134GM01
38. Fu, D., & Prein, A. F. (2026). Evaluation and future changes of mesoscale convective systems over the conterminous United States in high-resolution global and regional simulations. Geophysical Research Letters, 53(13), e2026GL122237. https://doi.org/10.1029/2026GL122237

39. Tsujino, H., Urakawa, S., Nakano, H., Small, R. J., Kim, W. M., Yeager, S. G., Danabasoglu, G., Suzuki, T., Bamber, J. L., Bentsen, M., Böning, C. W., Bozec, A., Chassignet, E. P., Curchitser, E., Boeira Dias, F., Durack, P. J., Griffies, S. M., Harada, Y., Ilicak, M., ... Yamazaki, D. (2018). JRA-55 based surface dataset for driving ocean-sea-ice models (JRA55-do). Ocean Modelling, 130, 79-139. https://doi.org/10.1016/j.ocemod.2018.07.002
40. Haarsma, R. J., Roberts, M. J., Vidale, P. L., Senior, C. A., Bellucci, A., Bao, Q., Chang, P., Corti, S., Fučkar, N. S., Guemas, V., von Hardenberg, J., Hazeleger, W., Kodama, C., Koenigk, T., Leung, L. R., Lu, J., Luo, J.-J., Mao, J., Mizielinski, M. S., ... von Storch, J.-S. (2016). High Resolution Model Intercomparison Project (HighResMIP v1.0) for CMIP6. Geoscientific Model Development, 9, 4185-4208. https://doi.org/10.5194/gmd-9-4185-2016
41. Danabasoglu, G., Lamarque, J.-F., Bacmeister, J., Bailey, D. A., DuVivier, A. K., Edwards, J., Emmons, L. K., Fasullo, J., Garcia, R., Gettelman, A., Hannay, C., Holland, M. M., Large, W. G., Lauritzen, P. H., Lawrence, D. M., Lenaerts, J. T. M., Lindsay, K., Lipscomb, W. H., Mills, M. J., ... Strand, W. G. (2020). The Community Earth System Model Version 2 (CESM2). Journal of Advances in Modeling Earth Systems, 12(2), e2019MS001916. https://doi.org/10.1029/2019MS001916
42. Ullrich, P. A., Zarzycki, C. M., McClenny, E. E., Pinheiro, M. C., Stansfield, A. M., & Reed, K. A. (2021). TempestExtremes v2.1: A community framework for feature detection, tracking, and analysis in large datasets. Geoscientific Model Development, 14(8), 5023-5048. https://doi.org/10.5194/gmd-14-5023-2021
43. Fu, D., Liu, X., Castruccio, F., Zhang, G., Chang, P., & Danabasoglu, G. (2025). Global warming amplifies inland compound risks from tropical cyclones. Research Square [Preprint]. https://doi.org/10.21203/rs.3.rs-7369582/v1
44. Fu, D., Chang, P., Patricola-DiRosario, C. M., Saravanan, R., Liu, X., & Beck, H. E. (2021). Central American mountains inhibit eastern North Pacific seasonal tropical cyclone activity. Nature Communications, 12(1), 4422. https://doi.org/10.1038/s41467-021-24657-w
45. Knapp, K. R., Kruk, M. C., Levinson, D. H., Diamond, H. J., & Neumann, C. J. (2010). The International Best Track Archive for Climate Stewardship (IBTrACS): Unifying tropical cyclone data. Bulletin of the American Meteorological Society, 91(3), 363-376. https://doi.org/10.1175/2009BAMS2755.1
46. Rayner, N. A., Parker, D. E., Horton, E. B., Folland, C. K., Alexander, L. V., Rowell, D. P., Kent, E. C., & Kaplan, A. (2003). Global analyses of sea surface temperature, sea ice, and night marine air temperature since the late nineteenth century. Journal of Geophysical Research: Atmospheres, 108(D14), 4407. https://doi.org/10.1029/2002JD002670
47. Hersbach, H., Bell, B., Berrisford, P., Hirahara, S., Horányi, A., Muñoz-Sabater, J., ... & Thépaut, J.-N. (2020). The ERA5 global reanalysis. Quarterly Journal of the Royal Meteorological Society, 146(730), 1999-2049. https://doi.org/10.1002/qj.3803
48. Baker, L. H., Shaffrey, L. C., Sutton, R. T., Weisheimer, A., & Scaife, A. A. (2018). An intercomparison of skill and overconfidence/underconfidence of the wintertime North

Atlantic Oscillation in multimodel seasonal forecasts. Geophysical Research Letters, 45(15), 7808-7817. https://doi.org/10.1029/2018GL078838

49. Murakami, H., Delworth, T. L., Cooke, W. F., Zhao, M., Xiang, B., & Hsu, P. C. (2020). Detected climatic change in global distribution of tropical cyclones. Proceedings of the National Academy of Sciences, 117(20), 10706-10714. https://doi.org/10.1073/pnas.1922500117

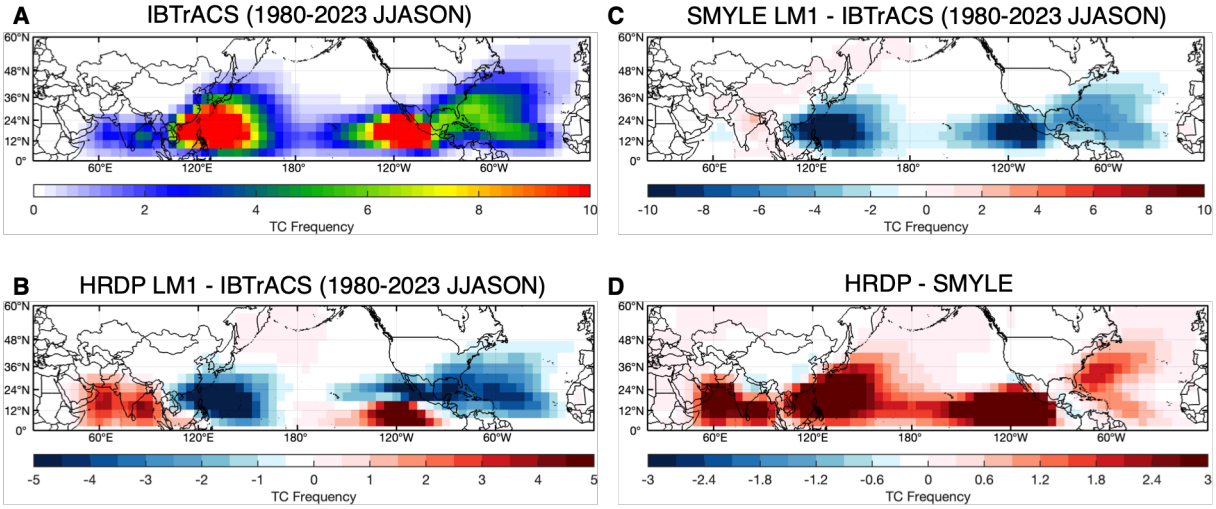
779 Supplementary Table 1. Comparison of HRDP and SMYLE prediction-system configurations.

	HRDP	**SMYLE**
Model	CESM1.3	CESM2
Ocean	POP2 (~0.1°, 62L)	POP2 (~1°, 60L)
Atmosphere	CAM5-SE (~0.25°, 30L)	CAM6-FV (~1°, 32L)
Land	CLM4 (~0.25°)	CLM5 (~1°)
Sea ice	CICE4 (~0.1°)	CICE5.1.2 (~1°)
Forcing	CMIP5	CESM2-LE / largely CMIP6
Scenario	Historical (1980-2005)+ RCP8.5 (2006-2023)	Historical (1980-2014) + SSP3-7.0 (2015-2023)
Initialization	Full field	Full field
Ocean	HR-FOSI (~0.1°, OMIP2; JRA55-do)	FOSI (~1°, OMIP2; JRA55-do)
Atmosphere	JRA55 reanalysis	JRA55 reanalysis
Land	HighResMIP Tier 1 atmosphere-land simulation	Forced CLM5 land-only simulation (CRU-JRAv2)
Sea ice	HR-FOSI (~0.1°, OMIP2; JRA55-do)	FOSI (~1°, OMIP2; JRA55-do)
Ensemble generation	Round-off-level perturbations to atmospheric potential temperature	Round-off-level perturbations to atmospheric potential temperature
Hindcasts used in this study	N = 44	N = 44
Start date	May 1	May 1
Start years	1980–2023	1980–2023
Simulation length	62 months	24 months
Ensemble size	10	20

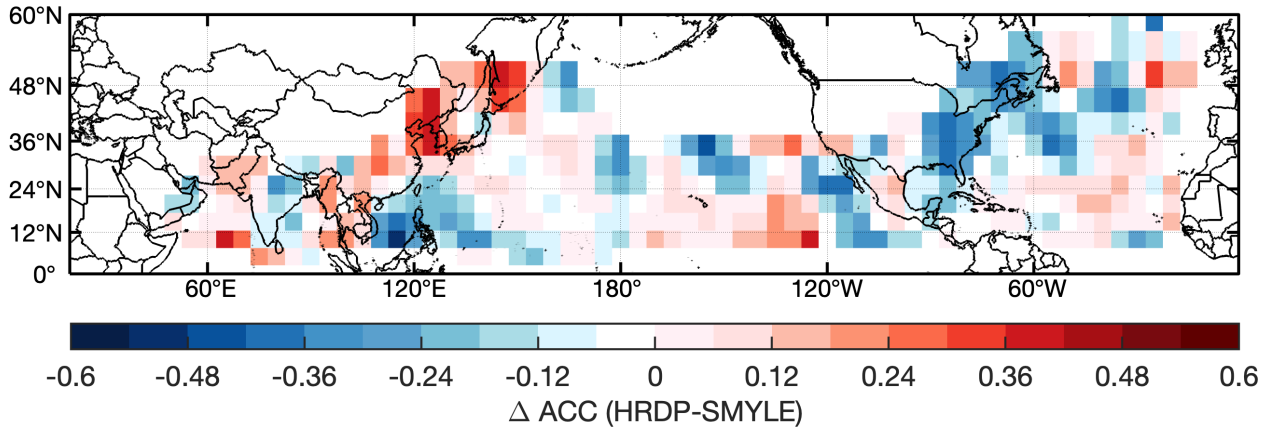
780

781

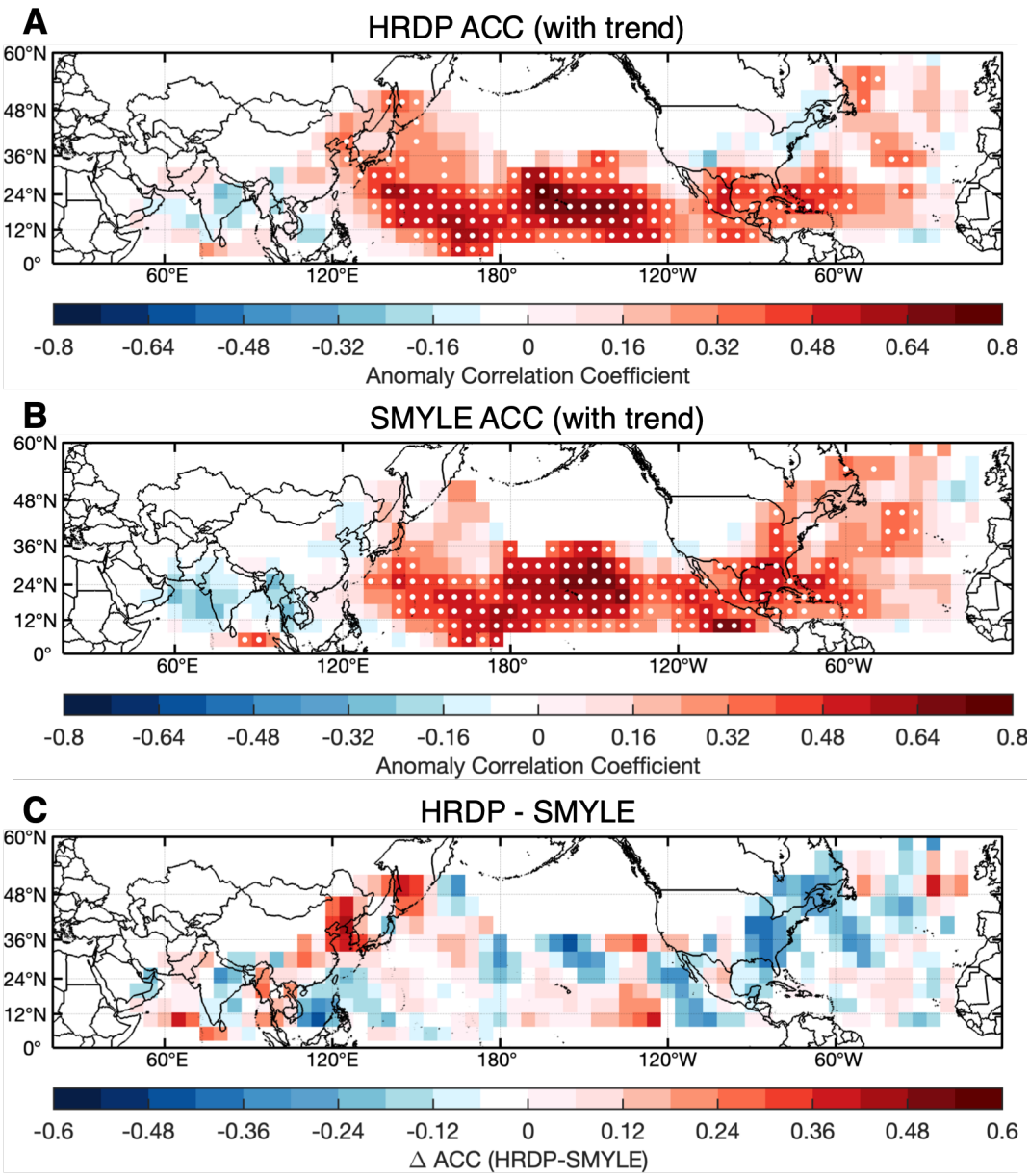
782



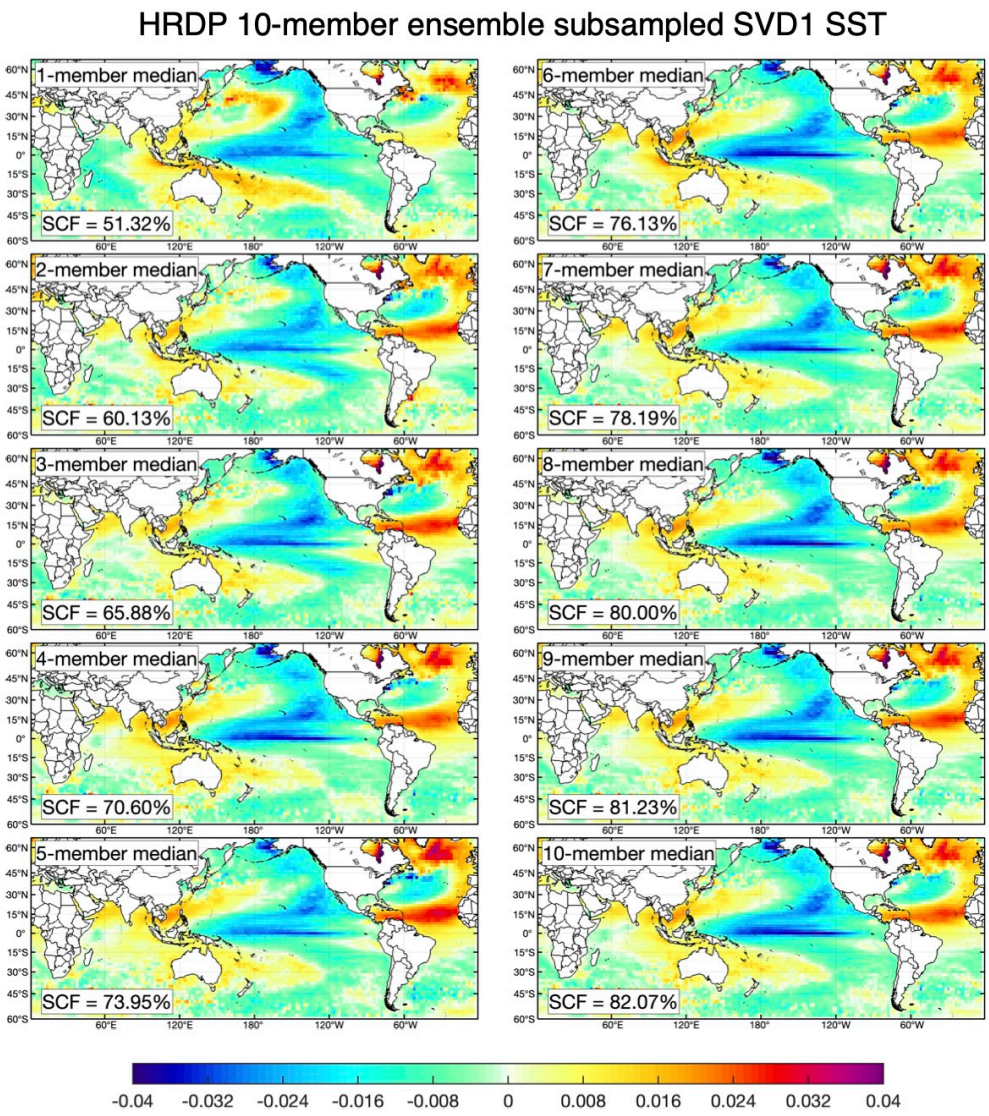
Supplementary Figure 1. Observed and simulated TC track density climatology and model biases. (A) Observed June–November (JJASON) TC track density from IBTrACS over 1980–2023. **(B)** Difference between the climatological TC track density in the May-initialized JJASON (lead month 1; LM1) HRDP hindcasts and IBTrACS. **(C)** As in **(B)**, but for SMYLE. **(D)** Difference in climatological TC track density between HRDP and SMYLE. Positive values in **(B–D)** indicate greater TC activity in the first dataset relative to the second, whereas negative values indicate lower activity. HRDP reproduces substantially more TC activity than SMYLE across most major Northern Hemisphere TC basins, although notable regional biases remain in both systems.



Supplementary Figure 2. Difference in seasonal TC track density prediction skill between HRDP and SMYLE. Difference in detrended anomaly correlation coefficient (ACC) between the May-initialized HRDP and SMYLE ensemble-mean predictions of June–November (JJASON) TC track density over 1980–2023. Linear trends are removed separately from the observed and predicted time series at each grid point before calculating the ACC. Positive values indicate higher prediction skill in HRDP, whereas negative values indicate higher skill in SMYLE.

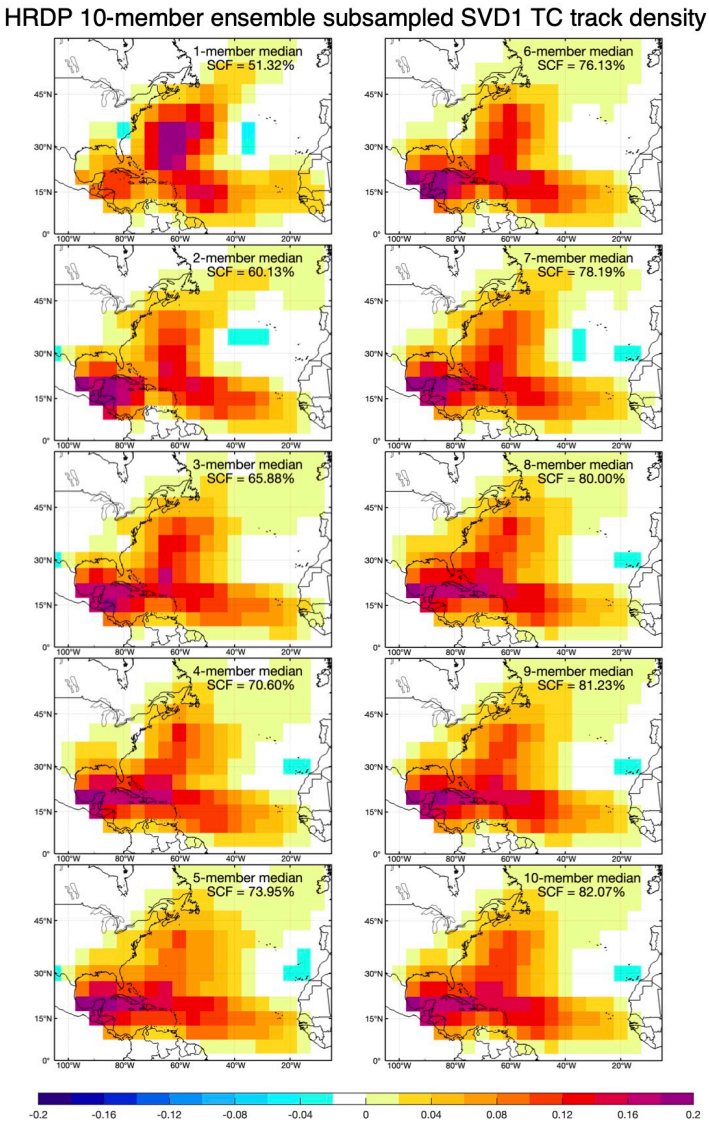


Supplementary Figure 3. Seasonal TC track density prediction skill without detrending. (A) ACC between observed and ensemble-mean JJASON TC track density from the May-initialized HRDP hindcasts over 1980–2023, calculated from the original time series without removing linear trends. White stippling denotes correlations statistically significant at the 95% confidence level. **(B)** As in **(A)**, but for SMYLE. **(C)** Difference in ACC between HRDP and SMYLE; positive values indicate higher prediction skill in HRDP, whereas negative values indicate higher skill in SMYLE.



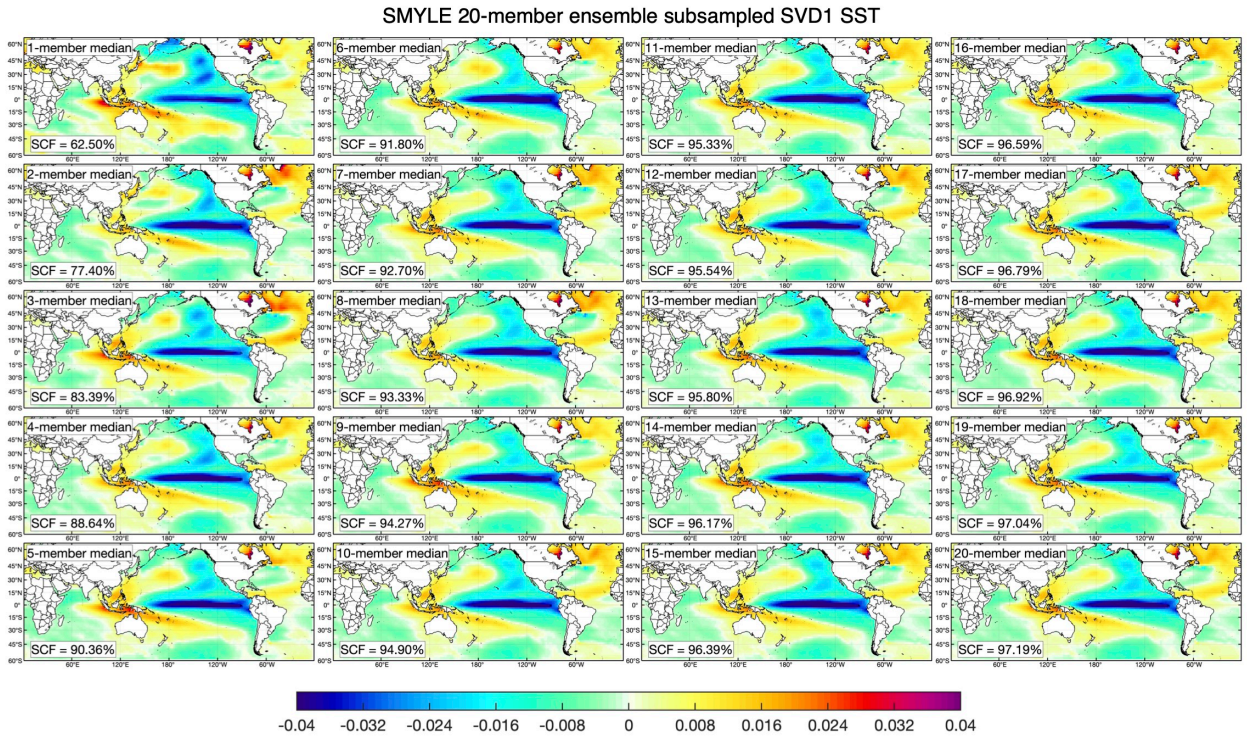
Supplementary Figure 4. Sensitivity of the HRDP SVD1 SST pattern to ensemble size. Leading SVD1 SST patterns obtained by subsampling the 10-member HRDP ensemble from 1 to 10 members. For each ensemble size, members are sampled without replacement; 1,000 random subsets are used when more than 1,000 unique combinations are available, whereas all possible combinations are used when the total number is smaller than 1,000. For each subset, the selected members are first averaged and SVD is then applied between the ensemble-mean SST and TC track density fields. Each panel shows the median SVD1 SST pattern across the subsamples for the indicated ensemble size. The annotated squared covariance fraction (SCF) denotes the median fraction of total squared SST–TC covariance explained by SVD1 across the corresponding subsamples. The increasing SCF with ensemble size indicates that ensemble averaging progressively isolates a dominant SST–TC covariance mode. See main text and Methods for details.

825

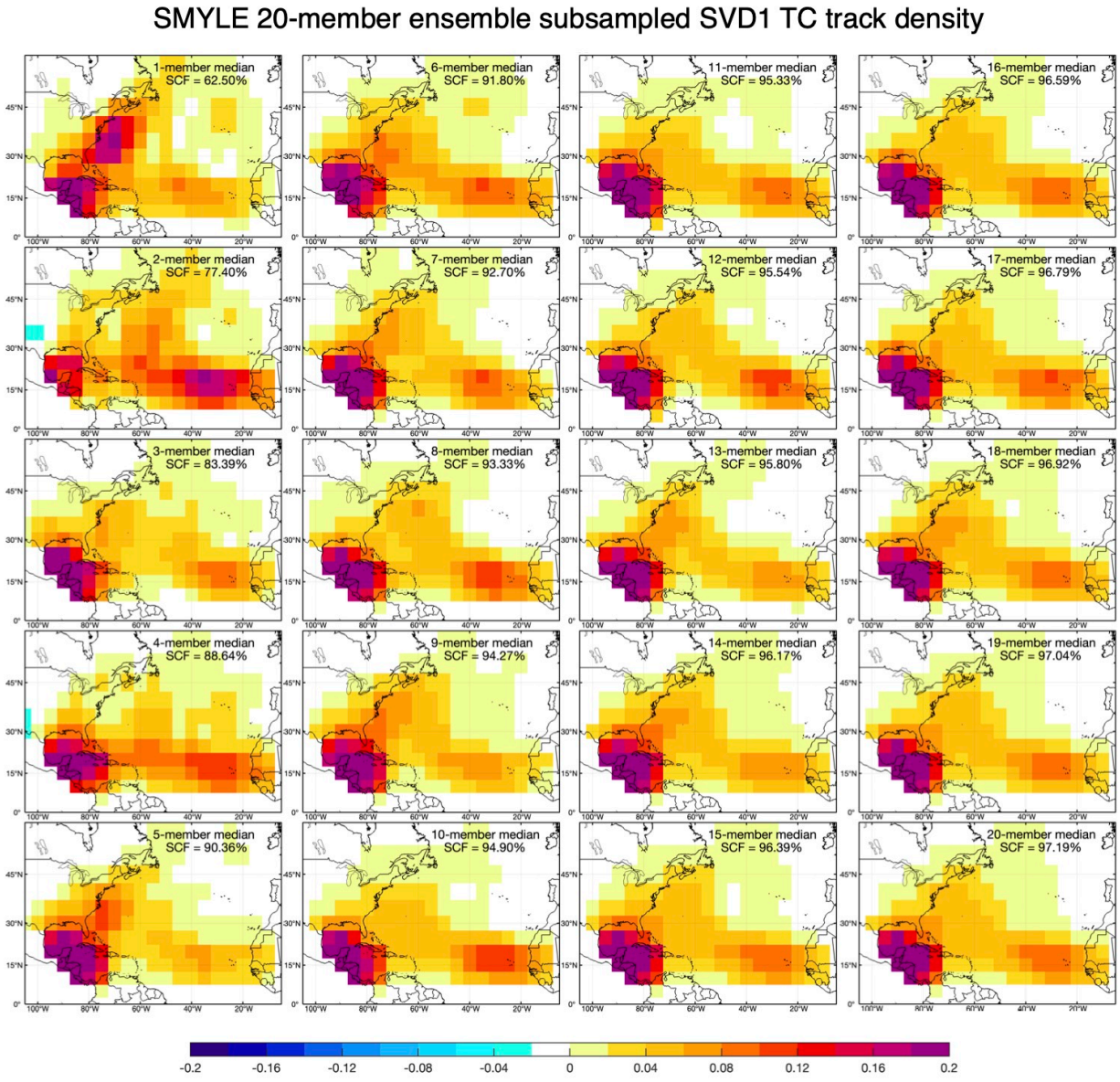


826

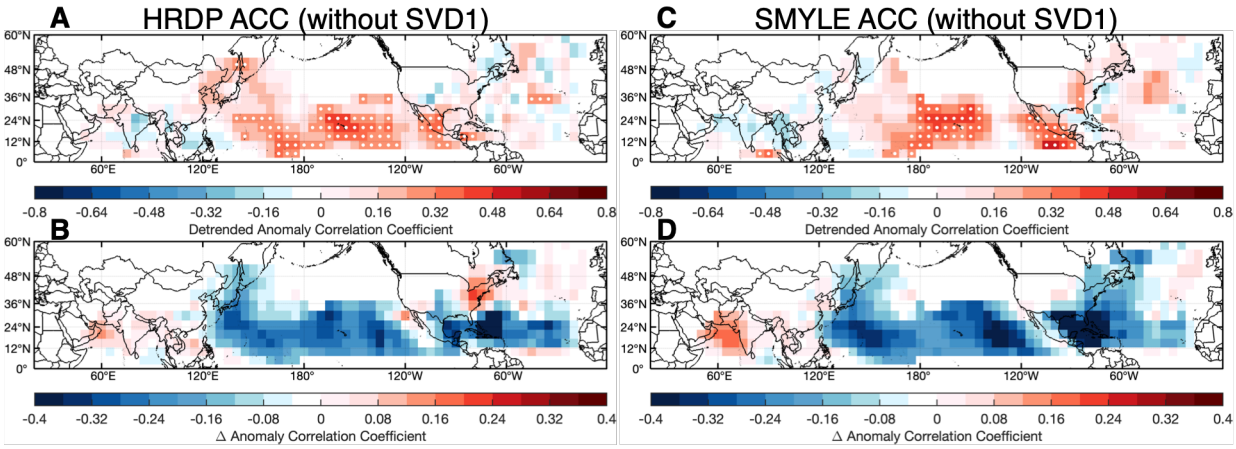
827 **Supplementary Figure 5.** Similar to Supplementary Figure 4, but for sensitivity of the HRDP
828 SVD1 TC track density to ensemble size



Supplementary Figure 6. Sensitivity of the SMYLE SVD1 SST pattern to ensemble size. As in Supplementary Figure 4, but for SMYLE using its 20-member ensemble.



Supplementary Figure 7. Sensitivity of the SMYLE SVD1 TC track density pattern to ensemble size. As in Supplementary Figure 5, but for SMYLE using its 20-member ensemble.



838

839 **Supplementary Figure 8.** Contribution of the leading coupled SST–TC mode to regional TC
840 prediction skill. (**A**) Detrended ACC between observed and ensemble-mean TC track density from
841 the May-initialized HRDP hindcasts over 1980–2023, after removing the TC-side SVD1
842 component from both the observed and predicted TC track-density fields. White stippling denotes
843 correlations statistically significant at the 95% confidence level. (**B**) Difference between the ACC
844 after removing TC-SVD1 and the original ACC in HRDP. Negative values indicate reduced
845 prediction skill after removal of the leading coupled mode. (**C,D**) As in (**A,B**), but for SMYLE.
846 The coherent negative ACC differences over the Gulf–Caribbean region in both systems indicate
847 that a substantial portion of the common regional prediction skill is concentrated in TC variability
848 represented by the leading SST–TC coupled mode.

849

850